p53 dynamics in response to DNA damage vary across cell lines and are shaped by efficiency of DNA repair and activity of the kinase ATM

Jacob Stewart-Ornstein and Galit Lahav*

Cellular systems show a wide range of signaling dynamics. Many of these dynamics are highly stereotyped, such as oscillations at a fixed frequency. However, most studies looking at the role of signaling dynamics focus on one or a few cell lines, leaving the diversity of dynamics across tissues or cell lines a largely unexplored question. We focused on the dynamics of the tumor suppressor protein p53, which regulates cell cycle arrest and apoptosis in response to DNA damage. We established live-cell reporters for 12 cancer cell lines expressing wild-type p53 and quantified p53 dynamics in response to double-strand break–inducing DNA damage. In many of the tested cell lines, we found that p53 abundance oscillated in response to ionizing radiation or the DNA-damaging chemotherapeutic neocarzinostatin and that the periodicity of the oscillations was fixed. In other cell lines, p53 abundance dynamically changed in different ways, such as a single broad pulse or a continuous induction. By combining single-cell assays of p53 signaling dynamics, small-molecule screening in live cells, and mathematical modeling, we identified molecules that perturbed p53 dynamics and determined that cell-specific variation in the efficiency of DNA repair and the activity of the kinase ATM (ataxia-telangiectasia mutated) controlled the signaling landscape of p53 dynamics. Because the dynamics of wild-type p53 varied substantially between cell lines, our study highlights the limitation of using one line as a model system and emphasizes the importance of studying the dynamics of other signaling pathways across different cell lines and genetic backgrounds.

INTRODUCTION

Many signaling pathways use complex dynamics to encode information about intensity, duration, and identity of a signal. The mechanism and differential outcomes of this encoding have received substantial attention, but less emphasis has been put on the conservation of these dynamics across different contexts or cell types. For example, pathways such as nuclear factor kappa-light-chain-enhancer of activated B cells (NF-κB), nuclear factor of activated T cells (NFAT), and extracellular signal–regulated kinase (ERK) all show complex time dynamics in mammalian cells after stimulus, but rarely has the diversity of these dynamics across tissues or cell lines been explored (1–3). The conservation of dynamical behaviors across cell lines encodes important information about the genetic or epigenetic underpinnings of these responses.

The dynamics of signaling pathways are increasingly seen as potential clinical targets for cancer therapy (4). Understanding the diversity and dose dependence of these dynamics is therefore crucial to predict potential toxicities in the body and which tumors may be sensitive to certain time scales of treatments. In addition, choosing appropriate model systems or cell lines to represent a relevant clinical spectrum of behavior is a challenging unsolved problem in basic research. Understanding the robustness of a dynamic behavior across cell types or cancer lines is therefore required for developing greater mechanistic insights into the conservation or dynamic range of specific features of various cellular systems.

Previous work on the response of the tumor-suppressing transcription factor p53 to DNA damage suggests that p53 signaling has dynamic properties that depend on the stimulus and can alter the outcome of DNA damage. In response to double-strand breaks, feedback loops cause p53 to oscillate in populations and individual cells (5, 6), a pattern of signaling compatible with both resumption of proliferation and permanent arrest if such oscillations persist. In contrast, non-oscillatory sustained activation

of p53 is associated with permanent cell cycle arrest (7). Although oscillatory expression of p53 has been observed in several cell types (8, 9) and in vivo (10), it is unclear if this represents a universal signaling pattern or a special case, and further, how these dynamics might play out in cancer cells with a compromised DNA damage response.

To explore the diversity in p53 signaling, we collected a set of 12 p53 wild-type tumor cell lines and quantified changes in p53 protein abundance in response to DNA damage in individual cells. We found that all 12 lines respond to DNA damage by activating functional p53. However, the dynamics of p53 varied greatly across cell lines. Furthermore, in some cell lines, the p53 response was largely dose-independent, whereas other lines showed dose-responsive behaviors. To identify what cellular features might lead to different p53 dynamics, we applied a targeted chemical screen for modifiers of p53 dynamics and determined DNA repair capacity and ATM (ataxia-telangiectasia mutated) signaling as the main dynamical regulators. Small-molecule inhibitors of ATM converted sustained p53 signaling to the classical pulsatile behavior, whereas inhibitors of DNA repair, or compounds that increase ATM activity, promoted sustained signaling. We codified our experimental findings in a mathematical framework that describes the "signaling space" of p53 across cell lines and various doses of DNA damage–inducing agents. Our study reveals that wild-type p53 shows different dynamical behaviors across cell lines, which are shaped by specific signaling states, and suggests pharmacological approaches to modulate these dynamics.

RESULTS

Different cell lines show comparable absolute p53 abundance but diverse p53 dynamics

To study the diversity in p53 response to DNA damage, we assembled 12 cell lines including 11 of the 14 National Cancer Institute 60 cell lines that are wild type for p53 (discarding three lines that posed difficulties for microscopy) and the widely used p53 wild-type osteosarcoma cell

Department of Systems Biology, Harvard Medical School, Boston, MA 02115, USA.
*Corresponding author. Email: galit@hms.harvard.edu

line U2OS. We acknowledge that this is not a random selection of cell lines, in part because it includes an overrepresentation of melanoma lines (5 of 12, owing to the relatively low rate of p53 mutations in melanoma). However, these lines represent a fairly typical range of immortalized cell lines that are widely used in cancer and DNA damage fields. The lines were treated with the radiomimetic drug neocarzinostatin (NCS), and p53 abundance was measured by immunofluorescence. NCS creates a burst of DNA double-strand breaks and was shown to act within 5 min after its addition to culture medium (*11*). All 12 lines showed comparable basal amounts of p53 (mean abundance within threefold), and after DNA damage, p53 abundance increased in every cell line from 1.25- to 5-fold (Fig. 1, A and B). Cell-to-cell variation was substantial in all lines, with damaged and undamaged populations overlapping in p53 abundance. This variation in p53 abundance is not likely the result of genetic inhomogeneity across a cell line because multiple clones obtained from two lines (HCT116 and A549) showed similar degrees of heterogeneity and relatively uniform responses to DNA damage (fig. S1).

To test the dependence of p53 induction on the extent of DNA damage, we quantified p53 abundance in response to a titration series of NCS in each cell line. We applied NCS in doses ranging from those that completely inhibit growth to those that cause minimal loss of proliferation (two orders of magnitude of NCS; fig. S2A) and measured p53 abundance after 2 hours (early response) and 8 hours (mid-response). In the A549 line, for example, we observed an initial increase in p53, which was comparable across all DNA damage doses (measurement at 2 hours; Fig. 1C). In contrast, the mid-response (at 8 hours) was graded, with a linear correlation between damage dose and p53 abundance (Fig. 1D). A similar picture was obtained for the other lines (Fig. 1, E and F), although we note that three of the melanoma lines (UACC257, SK-MEL5, and MALME3) showed a slight dose dependency at the 2-hour time point. Together, these results suggest that p53 initial induction is switch-like, whereas the later response is more dose-dependent. This is consistent with an "emergency" DNA damage signaling system that initially responds at maximum strength regardless of the insult strength, whereas the mid–time point reflects the contribution of DNA repair and transcriptional feedback loops regulating p53 (*12*).

The major feedback mechanism that attenuates p53 is its transcriptional target gene encoding the E3 ligase MDM2 (*5*, *13*). To quantify the p53-MDM2 feedback in all 12 lines, we measured the abundance of p53 and MDM2 at the early (2-hour) and mid- (8-hour) response to DNA damage (NCS) by immunofluorescence. In the early response, we observed an increase in p53 and a minimal change in MDM2 across all cell lines (Fig. 2, A and B). In the mid-response, all cell lines showed an increase in MDM2 abundance, suggesting that p53 transcriptional activity is intact (Fig. 2B and fig S2B). The abundance of cyclin-dependent kinase (CDK) inhibitor CDKN1A (also known as p21), encoded by a second p53-dependent gene, also increased after DNA damage in all cell lines (fig. S2C). At 8 hours, the change in p53 abundance varied substantially, with increases in some lines and losses in others (Fig. 2A). Time course measurements of p53 abundance in fixed MCF7, A549, and HCT116 cells, which were assayed at additional intermediate (5 hours) and late (24 hours) time points, suggested different dynamical behaviors of p53 in these three lines (Fig. 2C): (i) an oscillatory pattern in MCF7 cells, (ii) a broader wave of activation in A549 cells, and (iii) a continuous accumulation in HCT116 (Fig. 2C). Analysis of these three representative cell lines suggests that p53 dynamics may vary considerably across cell lines.

Live-cell measurement of p53 dynamics shows cell line–specific behaviors

To further examine p53 dynamics across cell lines, we constructed live-cell reporters by transducing an exogenous allele of p53 tagged with yellow fluorescent protein
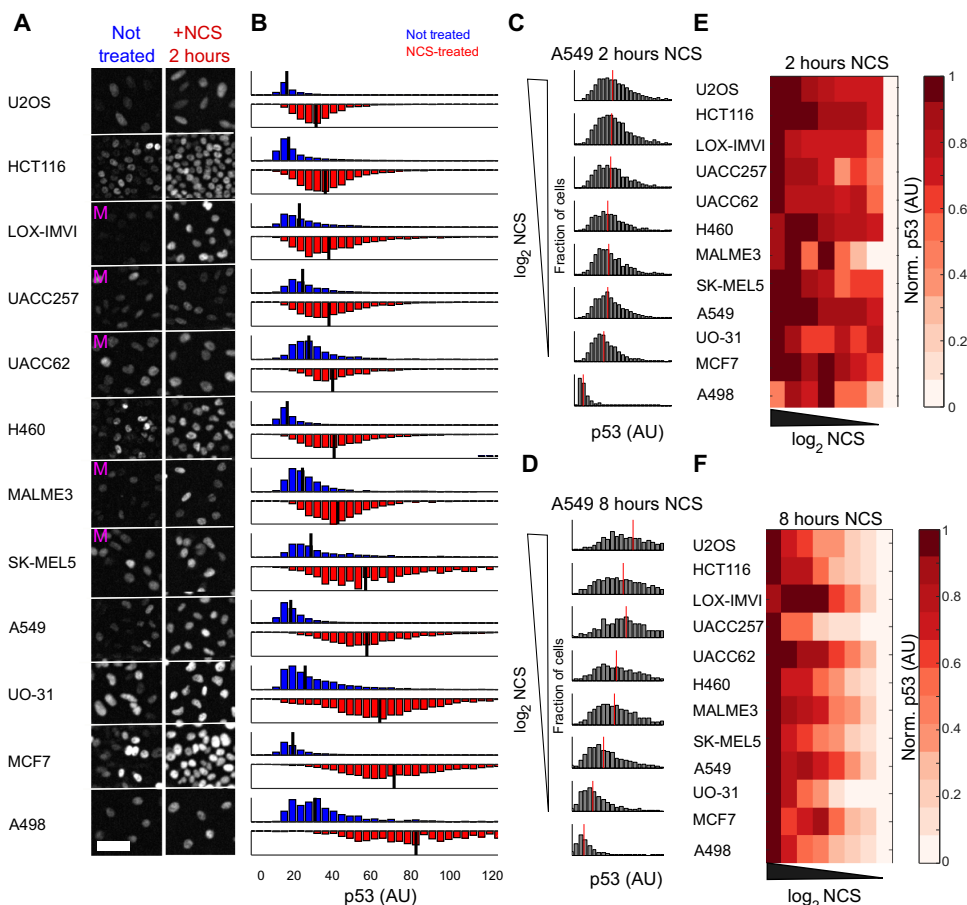

Fig. 1. p53 abundance and the initial response to DNA damage are comparable across cancer cell lines. (**A**) Twelve cell lines were stained for p53 before or 2 hours after treatment with the DNA-damaging agent NCS (100 ng/ml). Scale bar, 50 μm. "M" marks the five melanoma lines. (**B**) Histograms of single-cell straining intensity of p53 before (blue) or after (red) treatment with NCS. Black lines indicate the medians of the distributions. Cells are ordered by their median p53 abundance after NCS. AU, arbitrary units. (**C** and **D**) A549 cells were stained for p53 at 2 hours (C) or 8 hours (D) after a log₂ titration series of NCS. Red lines indicate the median of the distribution. Variation in p53 abundance across doses was assessed by unpaired *t* tests: $P > 0.05$ at 2 hours; $P < 0.05$ at 8 hours. (**E** and **F**) Each cell line was stained for p53 at 2 hours (E) or 8 hours (F) after varying doses of NCS. Heat maps represent p53 abundance. Each cell line was internally normalized (Norm.) between 0 and 1. Data in (B) to (F) are representative of two independent experiments ($n > 500$ cells for each cell line).

(p53-YFP) into each of the 12 cell lines. We selected stably expressing clones for each line (with the exception of LOX-IMVI, for which we were unable to obtain a single-cell clone and used an enriched polyclonal population) and assayed p53 dynamics in response to DNA damage by live-cell microscopy (Fig. 3A). For these experiments, we used ionizing radiation (IR) to induce DNA damage because it offered better day-to-day reproducibility than NCS across a wide range of doses. MCF7 cells showed sustained pulses of p53 after exposure to 6-Gy IR and one pulse after exposure to 1-Gy IR (Fig. 3B). In contrast, A549 cells showed more complex dose-dependent dynamics, with cells pulsing regularly after 1-Gy IR but showing a broader p53 pulse after 6 Gy (Fig. 3B). To examine the dependency of p53 dynamics on the radiation dose across cell lines, we exposed each line to five doses of IR (1, 2, 4, 6, and 8 Gy) and imaged single cells for 24 hours. Individual cells were tracked over time for p53 abundance and cell division events. These doses of radiation were sufficient to markedly suppress cell growth (Fig. 3C). Specifically, all cell lines showed a large fraction of actively dividing cells after exposure to 1-Gy IR, with that fraction declining as the dose of IR increased. Only a few cell lines showed notable division

at 4 Gy, and no divisions in any cell line were observed after exposure to ≥6 Gy (Fig. 3C).

All cell lines showed induction of p53 in response to radiation. However, as suggested by our experiments in fixed cells (Fig. 2), its dynamics varied considerably between the cell lines. This variation was independent of the tissue of origin because the five melanoma lines we studied showed a range of p53 dynamics. Our analysis revealed one major group of cell lines with periodic p53 pulses at low DNA damage and a more variable response at higher doses (Fig. 3D, top seven cell lines). The remaining cell lines were more heterogeneous, showing either a sustained response to DNA damage (A498 and SK-MEL5), a single non-oscillatory pulse (LOX-IMVI and HCT116), or mixed low-amplitude dynamics (MALME3). Focusing on the seven lines that showed clear oscillatory behavior, we noted that most of them (six of seven), like A549 cells, showed decreased oscillations and increased amplitude of p53-YFP at higher IR doses (and presumably greater extent of DNA damage), largely converting to a single broad peak by 8 Gy.

To quantify the periodic behavior of p53 in each cell line, we computed autocorrelation functions for each cell and averaged them to derive the mean periodicity of a cell line (Fig. 3E). The seven visually oscillatory lines showed a peak in the autocorrelation function at ~5 hours, consistent with previous reports for p53 oscillatory frequency (6). The uniformity of oscillation frequency suggests that common feedback loops govern the behavior of each cell, consistent with the universal induction of the feedback regulator MDM2 we observed (Fig. 2). This analysis also recapitulated the loss of periodicity in cell lines as IR dose increases, with some cell lines gradually transitioning from a principally oscillatory response to a more sustained response (A549 and U2OS) and other cell lines showing a stark transition at 6 Gy to a more sustained behavior (UO-31, UACC257, and H460). Uniquely, in this data set, MCF7 cells become more pulsatile over time, with cells treated with 1 Gy showing very little oscillatory behavior and higher doses producing increased periodicity.

In addition to loss of periodicity, increased doses of IR resulted in broader pulses of p53 activity in some cell lines. We computed the full width at half maximum (FWHM) of the first p53 pulse for each cell line across doses (Fig. 3F). A few lines (such as MCF7 and UACC257) showed relatively little change in FWHM with dose, whereas many of the lines that showed reduced oscillations at high doses showed dose-dependent increases in FWHM (H460, A549, and U2OS). In addition, the cell-to-cell variability of FWHM varied markedly between cell lines, ranging from exceptionally constrained (MCF7) to fairly broad (A549 and U2OS).

We further classified the 12 cell lines according to their dose-dependent periodicity by comparing the periodicity of each line at 1- and 8-Gy IR (Fig. 3G). We found that low-periodicity lines are not greatly affected by the IR dose (blue group), whereas high-periodicity lines tend to show reduced oscillations at high doses (green group). The exception was MCF7, which, as noted earlier, becomes more pulsatile as IR dose increases. These results underscore the complexity of p53 dynamics and their dependence on cell line identity, extent of DNA damage, and cell-to-cell heterogeneity.
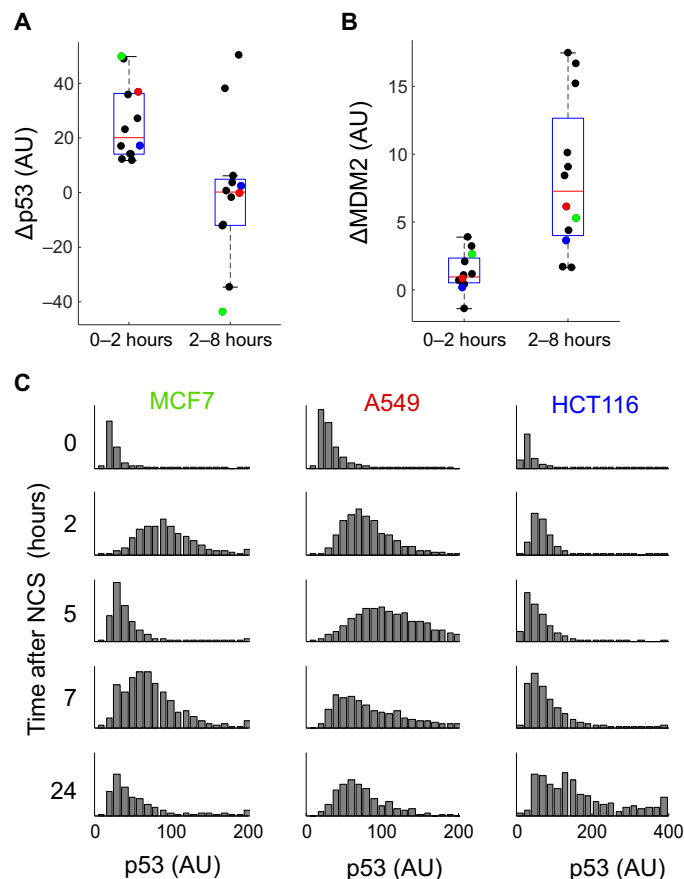

Fig. 2. p53 shows different temporal patterns across cell lines. (A and B) Abundance of p53 and MDM2 was quantified by immunofluorescence and is plotted as boxplots showing the change (Δ) in protein abundance between the 0- and 2-hour time points or between the 2- and 8-hour time points after NCS treatment (100 ng/ml). Dots represent each of the 12 cell lines, highlighting MCF7 (green), A549 (red), and HCT116 (blue). (C) Abundance of p53 quantified by immunofluorescence at the indicated time points after NCS treatment. Histograms from the three cell lines are shown. Data in (A) to (C) are representative of two independent experiments (n > 500 cells for each cell line).

Small-molecule kinase inhibitor screen identifies modulators of p53 dynamics

Our results suggest that the p53 signaling in human cancer lies on a continuum ranging from pulsatile to linear accumulation. Because of the large number of genetic lesions in each line studied here, we lacked the statistical power to infer which mutations or modifications might

contribute to the differential dynamics of p53 across cell lines. We therefore sought to identify modulators of p53 dynamics by screening for small molecules that alter p53 dynamics in one cell line. We used the U2OS p53 reporter line, which was intermediate in p53 response dynamics with both pulsatile (at low IR) and more sustained dynamics (at high IR; Fig. 3D), and showed low cell movement, making it suitable for automated analysis. The reporter line was plated in 96-well plates,

pretreated with a selection of small molecules for 2 hours, and then treated with NCS to induce DNA damage and imaged for 24 hours (Fig. 4A). Automated analysis identified ~100 to 200 cells in each well capable of being tracked for the duration of the movie for an average of ~15,000 single-cell traces per experiment. To explore cell signaling space, we used a collection of 178 small-molecule kinase inhibitors from the Library of Network-Based Cellular Signatures (LINCS) consortium (table S1).
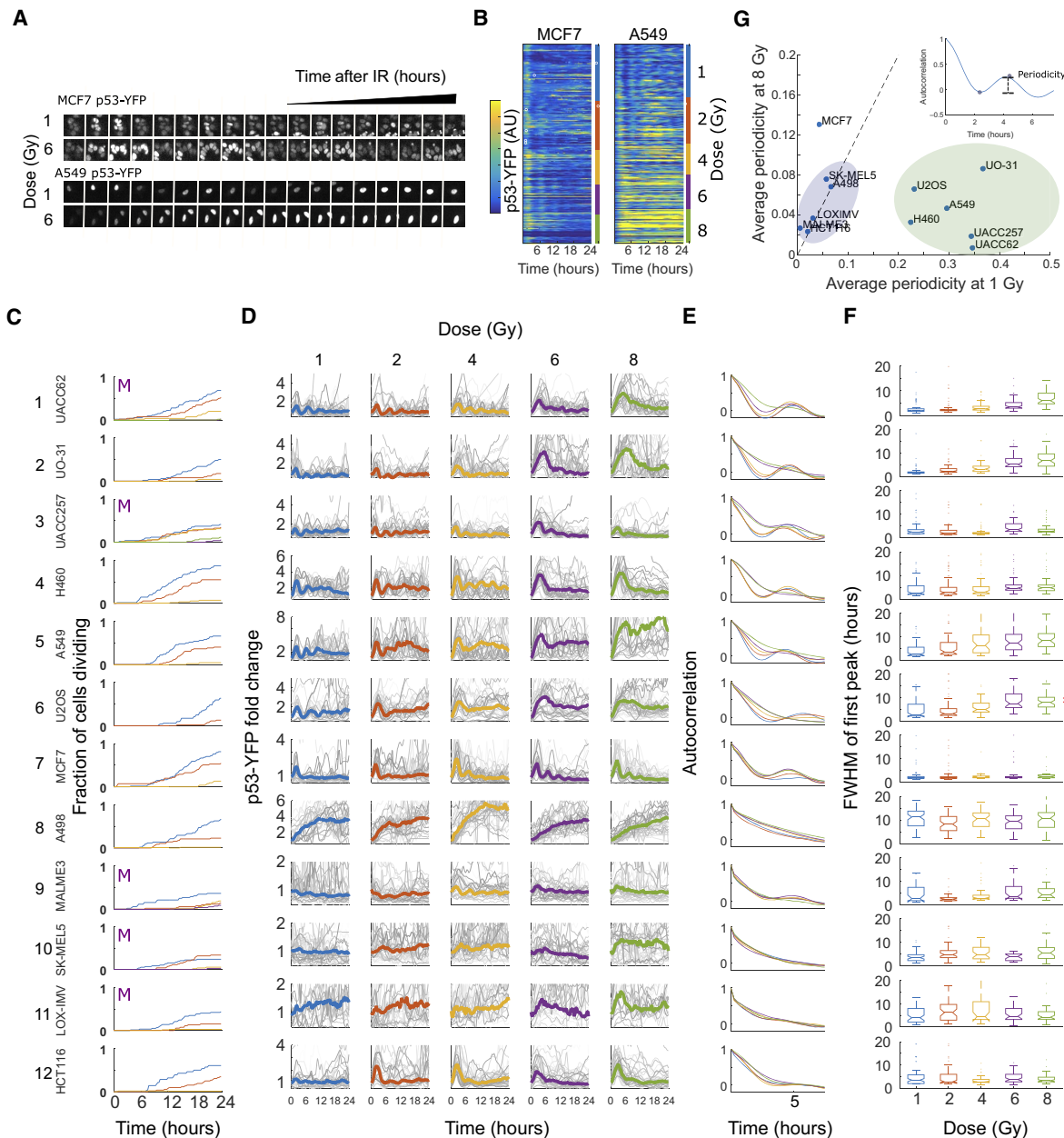

Fig. 3. Live-cell tracking of p53 over time reveals cell line–specific dynamics and dose dependency. (**A**) Images of MCF7 and A549 cell lines expressing p53-YFP over 18 hours after 1- or 6-gray (Gy) IR exposure. Scale bar, 50 μm. (**B**) Heat maps of p53-YFP abundance in MCF7 and A549 cells after exposure to various doses of IR. Each row represents a single cell. (**C** to **F**) Twelve cell lines were constructed to express p53-YFP and imaged after exposure to IR: 1 Gy, blue line; 2 Gy, red line; 4 Gy, yellow line; 6 Gy, purple line; 8 Gy, green line [or boxplot in (F)]. Data are from $n > 50$ cells for each condition (3825 cells in the full data set; pooled from two to three experiments for each line). "M" indicates melanoma cell lines. Measured for each dose in each cell line were the fraction of cells that have divided at a given time (C), p53-YFP abundance (bold colored lines, averages; gray lines, single-cell traces) (D), average autocorrelations of p53 trajectories (E), and the FWHMs of the first p53 pulse (boxplots show the distribution over single cells; asterisks indicate cell lines where the FWHM is dose-dependent; $P < 0.05$, t test) (F). (**G**) A measure of periodicity (maximum of autocorrelation function minus the minimum of autocorrelation function in the first 5 hours; see inset) was calculated for each cell line and condition.
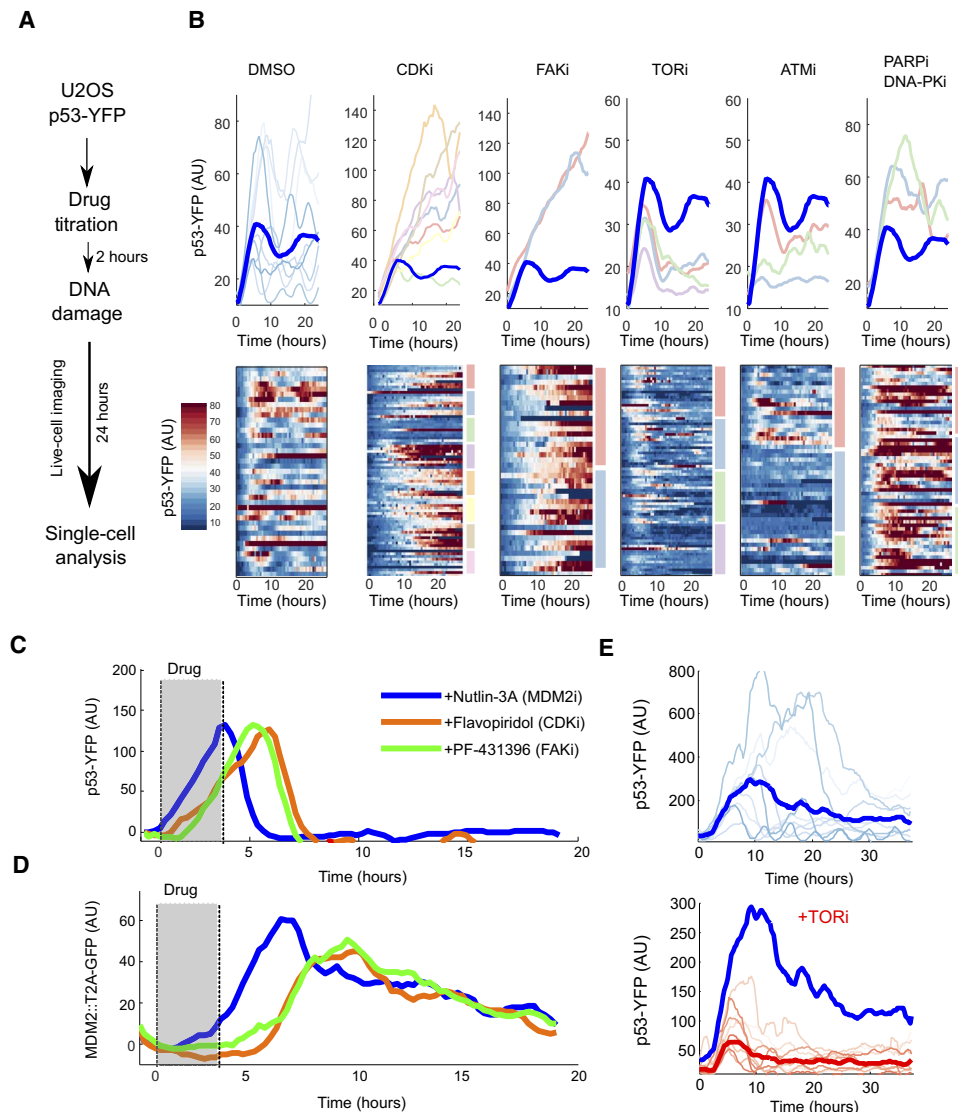
Fig. 4. A kinase inhibitor screen in live cells identified compounds that alter p53 dynamics after DNA damage. (**A**) Screen workflow in which U2OS cells expressing p53-YFP were incubated for 2 hours with kinase inhibitors and then exposed to NCS (100 ng/ml), followed by live-cell imaging of p53-YFP abundance over 24 hours. (**B**) Effect of pretreatment with various signaling molecule inhibitors on NCS-induced p53-YFP dynamics in U2OS cells. In the control graph [dimethyl sulfoxide (DMSO); far left], the bold blue line is the average trace, and the gray lines are single-cell traces. Each graph then shows the control trace as a reference (bold blue trace) alongside colored traces representing the average trajectory of p53-YFP abundance in cells exposed to specific compounds within each class of drug [each of eight CDK inhibitors (CDKi), two FAK inhibitors (FAKi), four mTOR inhibitors (TORi), three ATM inhibitors (ATMi), and four distinct combinations of two PARP (PARPi) and two DNA-PK inhibitors (DNA-PKi)]. Bottom: Heat maps of p53-YFP abundance in single U2OS cells after treatment with NCS (100 ng/ml) and the corresponding drug treatment (color-coded groups correspond to the traces above) ($n > 20$ cells for each condition). (**C** and **D**) Abundance of p53-YFP (C) or the transcriptional reporter MDM2::T2A-GFP (green fluorescent protein) (D) in transfected MCF7 cells exposed to a 3-hour pulse (shaded) of the MDM2 inhibitor (MDM2i) nutlin-3A, the CDK inhibitor flavopiridol, or the FAK inhibitor PF-431396. (**E**) Abundance of p53-YFP in A549 cells treated with either NCS (100 ng/ml; single-cell traces in gray, average in bold) (top) or the mTOR inhibitor AZD8055 and then NCS (blue, NCS-only trace inserted for reference) (bottom). Data in (C) to (E) are from $n > 25$ cells, representative of two experiments.

Analysis of our screening data revealed three major classes of p53 modulators: accelerators, which increased p53 abundances markedly [namely, inhibitors of CDK, focal adhesion kinase (FAK), and MDM2]; mild enhancers, which increased p53 abundances moderately [inhibitors of DNA-dependent protein kinase (DNA-PK), poly(adenosine

5′-diphosphate–ribose) polymerase (PARP), and glycogen synthase kinase 3β (GSK3β)]; and dampeners, which reduced p53 and caused the cells to show a more pulsatile behavior [inhibitors of ATM and mammalian target of rapamycin (mTOR)] (Fig. 4B and table S1).

We first explored the role of CDK inhibitors on p53 dynamics. Relatively high concentrations (2 μM) of seven of the eight CDK inhibitors we tested stabilized p53-YFP abundance in U2OS cells (Fig. 4B). The CDK inhibitors roscovitine and flavopiridol were previously reported to increase p53 concentrations because of reduced transcription of *MDM2*, likely through inhibition of CDK7 or CDK9, which are part of the general transcriptional machinery (*14*, *15*). Inhibition of FAK led to similar p53 behavior as observed after CDK inhibition (Fig. 4B), suggesting that FAK inhibitors may also induce p53 through loss of *MDM2* transcription. Quantitative polymerase chain reaction (qPCR) measurements showed that abundance of the MDM2 transcript dropped more than threefold after treatment with flavopiridol or PF-431396 (an FAK inhibitor) (fig. S3A).

To investigate the putative effect of CDK and FAK inhibitors on *MDM2* transcription and subsequently on p53 induction, we deployed a reporter for measuring *MDM2* transcription in live cells (MDM2::T2A-GFP) (*16*) and quantified its dynamics together with that of p53-YFP in MCF7 cells. Both flavopiridol and PF-431396 led to an increase in p53-YFP, likely due to depletion of MDM2 (Fig. 4, C and D). Once the drugs were washed out, *MDM2* transcription increased rapidly, followed by depletion of p53 (Fig. 4, C and D). These drugs both acted with a delay when added or washed out compared to the direct MDM2 inhibitor nutlin-3A, diagnostic of their slower transcriptional mechanism of action. These results show that CDK inhibitors and FAK inhibitors likely activate p53 through inhibition of *MDM2* transcription.

As opposed to CDK and FAK inhibitors, mTOR and ATM inhibitors dampened p53 activity in our screen (Fig. 4B). ATM is well known to play a major role in the induction of p53 in response to DNA damage (*17*, *18*), and we have thoroughly investigated the role of ATM on p53 dynamics across cell lines (see below). With regard to mTOR, we first verified that, as in U2OS cells, mTOR inhibitors lead to suppression of p53 in a second cell line (A549; Fig. 4E). Next, because mTOR and ATM are from the same family of phosphatidylinositol (3,4,5)-trisphosphate kinases, we

asked whether the mTOR inhibitors we used might also inhibit ATM activity in this context. Focusing on the highly specific clinical mTOR inhibitor AZD8055, we observed little decrease in the phosphorylation checkpoint kinase 2 (CHK2) at doses that had substantially altered p53 abundance (fig. S3B and table S1), arguing that perturbation of p53 dynamics by the mTOR inhibitor is not mediated through the ATM-CHK2 pathway. One other aspect of loss of mTOR signaling is a general translational attenuation. Cells treated with AZD8055 had decreased basal abundance of p53 1 hour after treatment, consistent with a translational block (fig. S3C). Such general translational attenuation may explain the damping of p53 activation we observed in mTOR-inhibited U2OS and A549 cells after DNA damage (Fig. 4, B and E). Although a specific link between mTOR signaling and p53 regulation would be intriguing, and such an interaction has been suggested (19), we are currently unable to decouple the potential specific activity of TOR inhibition on p53 from its general translational effects.

The fraction of unrepaired DNA breaks varies between cell lines

We next focused on the effect of inhibiting DNA-PK, PARP, or GSK3β on p53 dynamics. We initially confirmed that, as in U2OS cells, these inhibitors increase p53 in a second cell line (A549; Fig. 5A). The three pathways targeted by these drugs have been implicated in DNA repair; DNA-PK and PARP inhibitors were shown to directly affect DNA repair, largely through nonhomologous end joining and single-strand break repair, respectively (20–22), whereas the effect of GSK3β was suggested to be more tangential, possibly through p53 (23, 24). DNA-PK inhibitors also alter p53 dynamics (17). We confirmed that inhibition of PARP with the clinical small-molecule olaparib substantially increased DNA damage measured by γH2AX intensity 6 hours after 10-Gy IR exposure compared to cells treated with IR alone (Fig. 5B). These results link the repair of DNA damage to p53 dynamics, suggesting that some of the variation we observed in p53 signaling dynamics across cell lines (Fig. 3D) might result from differences in DNA damage repair capacity. We therefore systematically measured repair capacities in our collection of 12 cell lines (Fig. 5, C to F, and fig. S4A). We found that the extent of DNA damage remaining at 24 hours after NCS treatment varied greatly between cell lines (Fig. 5, C to F). Some cell lines, such as MCF7 and U2OS, showed almost complete repair with only a small fraction of DNA damage (γH2AX signal) persisting (<10%). Other lines such as HCT116 or A549 showed incomplete repair, with DNA damage stabilizing at roughly 30% its peak value and persisting for at least 24 hours (Fig. 5, D and F, and fig. S4A).

We next tested whether the unrepaired fraction of DNA damage was a dose-dependent phenomenon by measuring the fraction of DNA damage remaining after 0.5 and 8 hours across an eight-point titration of NCS treatment. We observed that most cell lines show a linear correlation between their maximal DNA damage and final DNA damage (Fig. 5E and fig. S4B). This result suggests that a fixed fraction of DNA damage is slow or difficult to repair for the cell and that the fraction of damage remaining is a dose-independent metric of cellular repair capacity for each cell line.

ATM activity varies greatly across cell lines

In addition to DNA repair inhibitors, ATM signaling also emerged from our screen as a major element shaping p53 signaling dynamics. The kinase ATM has been shown to phosphorylate p53 and MDM2, leading to stabilization of the p53 protein (16, 25). We therefore asked whether ATM activity plays a role in shaping p53 dynamics. We assessed ATM activity in each cell line after DNA damage by titrating the specific and stoichiometric ATM inhibitor (KU55933), measuring the resulting pCHK2 abundances, and normalizing them to no ATM inhibitor conditions in each cell line (Fig. 6A). This assumes similar drug penetrance in each cell line and uses the inhibitory concentration as a proxy for the quantity of ATM activity. Using this metric, we found that ATM activity after DNA damage varies widely across cell lines, with
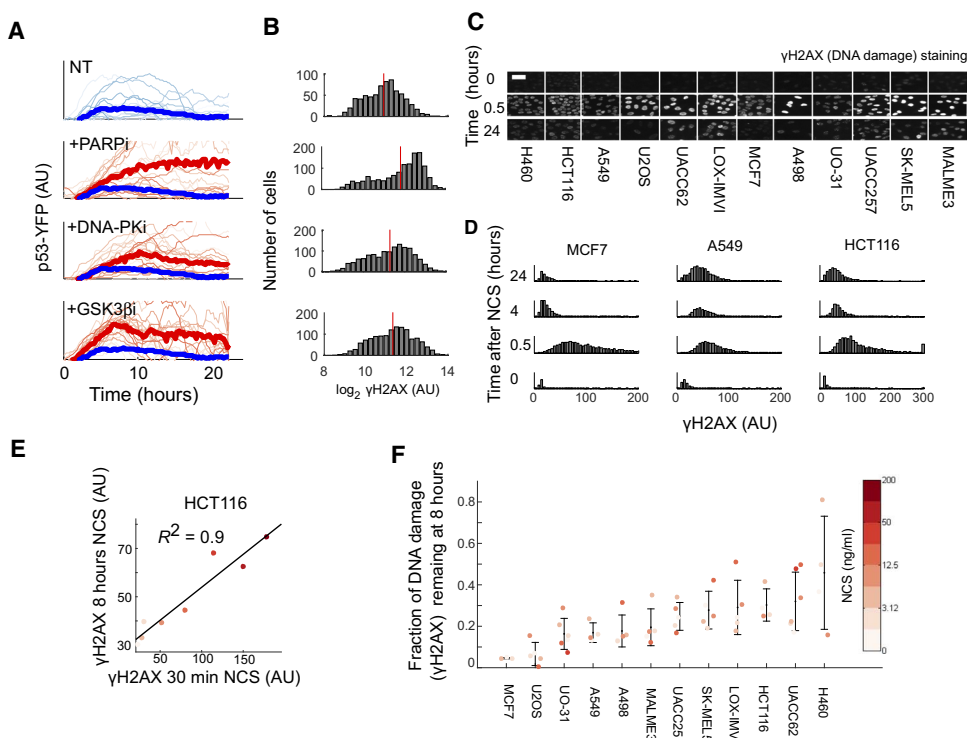

Fig. 5. Repair proficiencies vary between cell lines. (**A**) A549 cells expressing p53-YFP were pretreated with DMSO (NT) or olaparib (PARPi; 10 μM), NU7026 (DNA-PKi; 10 μM), or CH99021 (GSK3βi; 10 μM) for 1 hour and then treated with NCS (100 ng/ml). Red lines represent the treated condition (thin lines, single cells; thick line, average), and the blue line represents the control (NT) cells Data are representative of two independent experiments (n > 40 cells). (**B**) Quantification of γH2AX intensity induced by NCS (100 ng/ml) was measured 6 hours after 10-Gy IR in A549 cells pretreated with DMSO (NT; 1 hour) or the indicated inhibitor (10 μM; 1 hour). Histograms are shown, with a red line indicating the median. Data are representative of three independent experiments (n > 500 cells; P < 0.05, t test). (**C**) Images of cells from the indicated lines stained for γH2AX before or 0.5 or 24 hours after NCS treatment (100 ng/ml). Scale bar, 25 μm. (**D**) Histograms of MCF7, A549, and HCT116 cells stained for γH2AX at the indicated time points after NCS treatment (n > 200 cells from two independent experiments). (**E**) γH2AX in HCT116 cells was quantified 30 min and 8 hours after NCS. (**F**) DNA damage assessed as γH2AX abundance at 30 min and 8 hours in the indicated cell lines was compared across a range of NCS concentrations (noted in the color scale). Data are means ± SD (n = 7).

our most pulsatile cell line, MCF7, showing low ATM activity and less pulsatile lines, such as U2OS or A549, showing stronger ATM activity (Fig. 6, A and B).

Therefore, we tested whether reducing ATM activity by treatment with ATM inhibitors could broadly convert sustained lines into displaying pulsatile behavior. Treatment with moderate concentrations of ATM inhibitor followed by induction of DNA damage altered endogenous p53 dynamics in several cell lines, rendering them more pulsatile (for example, A549, A498, and UACC257; Fig. 6C). We further explored the dynamics of p53 in single A549 cells and found that single cells became pulsatile after DNA damage in the presence of moderate ATM inhibition (Fig. 6D). In contrast, when we increased ATM signaling in the normally highly pulsatile MCF7 cells by treating them with an inhibitor of a critical ATM phosphatase, PPM1D, we observed extended and less pulsatile p53 signaling (Fig. 6E), consistent with previous results using genetic perturbation of PPM1D (15). These results suggest that ATM activity is a crucial regulator of p53 dynamics and explains the nonpulsatile p53 behavior observed in some lines at higher DNA damage doses.

The variation in DNA repair efficiencies and ATM activities can explain the dynamical space of p53 across cell lines

To codify our insights into the regulation of p53 dynamics by DNA repair and ATM signaling, we constructed a model of p53 signaling and ran simulations with a range of ATM activities and DNA repair efficiencies (Fig. 7A). Consistent with our experimental observations, our model showed periodic signaling in a wide range of conditions, with low ATM activity or high DNA repair efficiency resulting in a single pulse or a few pulses. Moderate ATM activity sustained p53 oscillations, and high ATM activity led to a much broader p53 peak. DNA damage dose moved cells along the ATM signaling axis, but note that repair efficacy is an intrinsic property of a cell line that is unaffected by dose (fig. S4). The combination of DNA repair efficiency and ATM activity therefore creates a signaling space in which different cell lines may occupy different regions (Fig. 7B). We suggest that a cell line's starting point in this signaling space will result in qualitatively different p53 signaling patterns in response to different doses of DNA damage. For example, A549 cells show moderate repair but high intrinsic ATM activity, which, at high DNA damage doses, pushes this cell line out of the oscillatory p53 signaling regime and into more sustained behavior. MCF7 cells, on the other hand, have low ATM activity and do not leave the oscillatory regime even at high DNA damage doses (Fig. 7B). Examining p53 amplitude in this signaling space shows that a range of p53 amplitudes are possible within the oscillatory regime, suggesting that gene expression regulated by dynamics and amplitude could coexist (Fig. 7B).

DISCUSSION

In response to DNA damage, p53 abundance rises rapidly, triggering a cascade of transcription enforcing cell cycle arrest and, if the damage is severe enough, committing the cell to a terminal fate. IR was shown to trigger oscillations of p53 in MCF7 cells, in the nontransformed RPE1 cells, and in live mice (6, 9, 10, 15). These oscillations were shown to depend on the feedback loop with the E3 ligase Mdm2. Because p53, MDM2, and the upstream kinase regulators Chk2 and ATM are among the most frequently mutated genes in cancer, we asked how the dynamics of the p53 pathway might have diverged in tumor lines. Focusing on the 12 lines expressing wild-type p53, which we have shown to be capable of regulating MDM2 transcription and therefore imposing feedback regulation, we investigated the variation on p53 dynamics across lines in response to DNA double-strand breaks.

Although some cell lines showed stable oscillations of p53, like MCF7 cells, others showed diverse behaviors from broad peaks to slow ramps. Further, we observed that although some cell lines have invariant behavior regardless of DNA damage dose, others are sensitive to the magnitude of damage and show both different durations of p53 activation and different dynamical patterns of p53 under different doses. Some dynamical behaviors were, however, highly conserved across all cell lines, most notably the fundamental period of p53 oscillations, which was a stable ~5 hours for all cell lines with detectable oscillations. This result constrains our understanding of how the p53 network varies across systems, arguing that
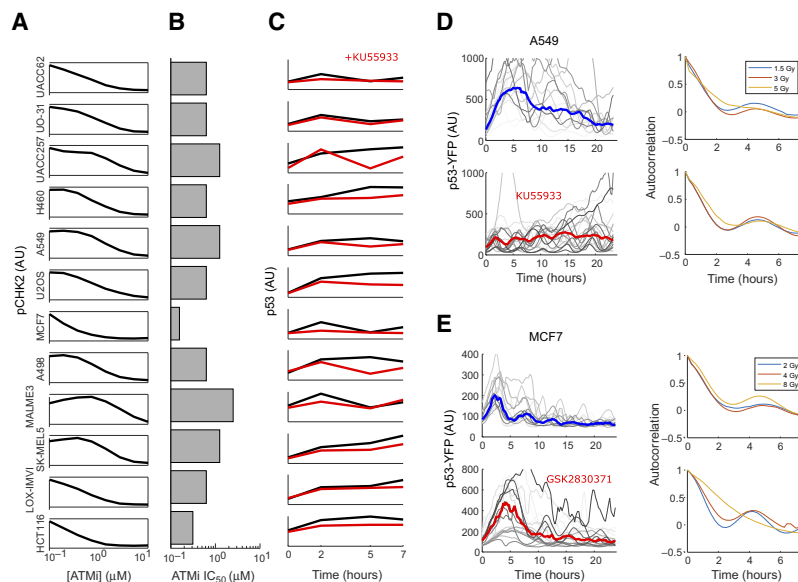

Fig. 6. ATM signaling varies across cell lines and manipulation of ATM modifies p53 periodicity. (**A**) ATM activity was quantified by immunofluorescence measurements of phosphorylated (p) CHK2 30 min after NCS (100 ng/ml) in the presence of one of the eight doses of ATM inhibitor KU55933. Data are shown as a lineplot, smoothed with a window of three. (**B**) The median inhibitory concentration (IC_{50}) of each cell line in response to ATM inhibition calculated from (A). (**C**) Mean p53-YFP abundance measured by immunofluorescence in each cell line treated with ATM inhibitor (2 μM; red) or DMSO (black) and at 2, 5, and 7 hours after NCS (100 ng/ml). Data are representative of three experiments (n > 200 cells). (**D** and **E**) Left: p53-YFP abundance in A549 cells exposed to 6-Gy IR (D) or MCF7 cells exposed to 8-Gy IR (E) in the presence (bottom) of DMSO (top) or ATM inhibitor (KU55933, 2 μM) (D) or PPM1D inhibitor (2 μM) (E). Right: Corresponding average autocorrelation curves (n > 50 cells, representative of two independent experiments).
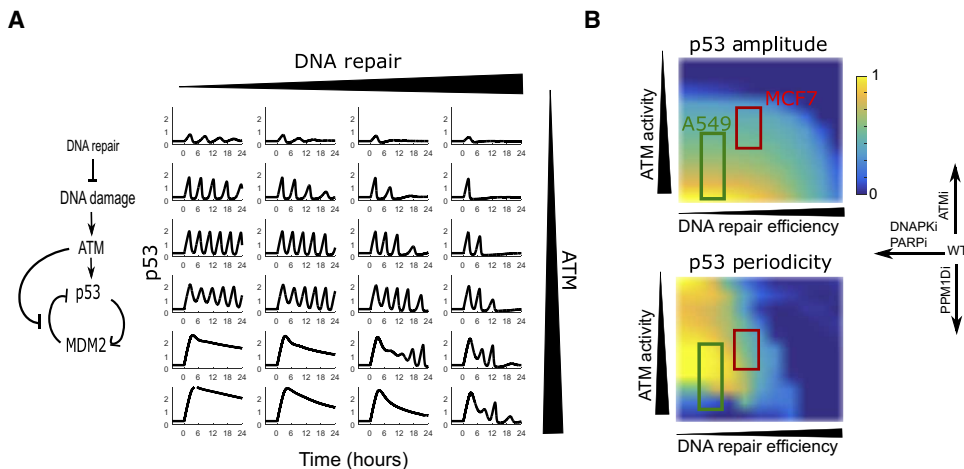
Fig. 7. ATM signaling and DNA repair capacity provide a range of p53 dynamical behaviors. (A) A computational model of p53 signaling was simulated with varying ATM activities and DNA repair efficiencies, resulting in a range of p53 dynamics capturing the experimental measurements in the different cell lines. **(B)** The maximum p53 amplitude and periodicity are shown as heat maps for various values of ATM activities and repair efficiencies. The putative "signaling spaces" in which MCF7 or A549 cells may reside are indicated, as are the effects of chemical inhibitors used in this study (right). WT, wild type; PPM1Di, PPM1D inhibitor.

ferent signaling outcomes. These results suggest that careful measurements of features such as ATM activity under baseline conditions may enable rational design of combination therapies to achieve specific cellular signaling dynamics in any given tumor.

Comparing p53 dynamics across tumor lines revealed an unexpected diversity of responses. Our work suggests that other dynamic regulatory signals, which were shown to have stereotyped behaviors (for example, NF-κB or ERK), may also vary substantially across cell lines, tumors, and tissues in the body. Combining single-cell reporters, batch immunofluorescence, and medium-throughput screening, as we used here to measure p53 dynamics across a diverse set of cell lines, will be essential for determining the conservation of dynamics in other signaling pathways and the machineries that permit this diversity.

the feedback circuit driving p53 oscillations is not greatly affected by tissue context but that upstream regulation of p53 signaling through ATM or other DNA damage signaling is.

Chemical and genetic screens have previously been used to look at the dynamics of circadian rhythms, leading to the identification of regulators responsible for maintaining the circadian period and amplitude (*25*, *26*). Here, we applied a similar live single-cell screening approach to identify kinase inhibitors that modify p53 dynamics. We identified several broad classes of inhibitors that modified p53 signaling, including ATM inhibitors, which converted p53 signaling from a broad peak to oscillations. This approach allowed us to examine the interaction between small-molecule inhibitors and DNA damage at high resolution. Because the dynamics of p53 signaling encode important information about both the nature of DNA damage and cell fate, such high resolution is critical. We suspect that as the technology for assaying molecular events inside cells and for high-throughput microscopy improves, such screens will become increasingly common.

Our small-molecule screen also revealed that inhibitors of mTOR, CDK, and PARP, all pathways targeted by cancer drugs currently in the clinic, also altered p53 activity. They appear to act through a mixture of DNA damage repair and global effects on transcription and translation. Notably, CDK inhibitors increased p53 abundance, likely by blocking MDM2 transcription (*18*), and although the p53 generated by CDK inhibition is likely harmless (because it cannot induce transcription in the presence of the drug), when the CDK inhibitor is washed away, p53 rapidly activates downstream targets to levels comparable to specific MDM2 inhibitors, suggesting that the activity of these compounds on p53 may depend greatly on pharmacokinetics of the specific small molecules.

Clinically applying combinations of DNA damage and small molecules to modify p53 signaling dynamics and treatment efficacy will require tumor-specific predicative modeling integrating the genotype of the tumor and the mechanism of each treatment modality. The model we developed here showed that depending on where a cell line starts in p53 signaling space, perturbations of ATM or DNA repair can result in dif-

MATERIALS AND METHODS
Cell culture
Parental cell lines were obtained from the American Type Culture Collection, thawed, and propagated in RPMI (Gibco) with 5% fetal bovine serum (FBS). All experiments were performed in this medium. For microscopy, RPMI lacking phenol red and riboflavin was used. For viral production, 293T cells were grown in Dulbecco's modified Eagle's medium (Gibco) + 10% FBS. All media were supplemented with 1% antibiotic and antimycotic (Corning). Cells from each line were infected with p53-YFP lentivirus in 35-mm dishes, selected with G418 (Sigma) of varying concentrations, and split into 96-well plates to select for clones expressing p53-YFP.

Immunofluorescence
Cells were plated in 96-well flat-bottom plates (Corning), grown for 24 to 48 hours, treated as indicated, and fixed with 2% paraformaldahyde (PFA) (Alfa Asear) for 10 min. Plates were washed twice with phosphate-buffered saline (PBS) and permeabilized with 0.1% Triton X-100 before sequential staining with primary and secondary antibodies. Cells were washed three times with PBS and imaged within 24 hours.

Virus production and infection
Virus was produced using 293T cells transfected with p53-YFP constructs, and viral packaging vectors and viral supernatant were collected after 3 days. For viral infection, Cells were plated at low density, and cells were infected with virus in medium containing Hepes and protamine sulfate. Cells were allowed to recover in nonselective medium for 1 day. Productively infected cells were selected with the appropriate antibiotic.

RNA extraction and quantitative reverse transcription PCR
Fifty thousand cells were plated in six-well plates. Cells were cultured for 24 hours and then treated with the indicated compounds. RNA was extracted by treatment with TRIzol and subsequent purification on a Zymo RNA column. The bulk RNA was reverse-transcribed using

the High-Capacity Reverse Transcription Kit (Applied Biosystems) to produce complementary DNA. Transcript abundance was quantified by specific primers for MDM2 using a SYBR Green–based (Life Technologies) qPCR and normalized to Actin.

Antibodies and reagents

Primary antibodies for p53 (FL393, Santa Cruz Biotechnology), MDM2 (SMP14, Santa Cruz Biotechnology), pCHK2 (Cell Signaling), γH2AX (JBW301, Millipore), p21 (Calbiochem), and Actin (Sigma) were obtained and used at 1:400 to 1:800. Secondary goat anti-mouse or anti-rabbit antibodies conjugated to AF555 or AF647 were purchased from Invitrogen. Small molecules were purchased from Enzo Life Sciences [flavopiridol (CDK1i)], Sigma [CH99021, NU7026 (DNA-PKi), and NCS], BioVision [AZD8055 (TORi)], Calbiochem [KU55933 (ATMi)], Life Technologies [4′,6-diamidino-2-phenylindole (DAPI)], and EMD Millipore [GSK2830371 (PPM1Di)]. X-ray–induced DNA damage was generated with an RS-2000 source (RadSource).

Microscopy

For live-cell imaging, cells were plated in glass-bottom 35-mm dishes (MatTek) 24 to 48 hours before imaging, and cells were switched to transparent medium (RPMI lacking riboflavin and phenol red, Invitrogen) 1 to 2 hours before imaging. Live-cell imaging was performed with a Nikon Ti microscope equipped with a heating chamber and a CO_2 source, an epifluorescent source [either a mercury arc lamp (Prior) or a light-emitting diode (LED) system (Lumencor)], an automated stage (Prior), a YFP filter set (Chroma), and a charge-coupled device (CCD) or complementary metal-oxide semiconductor (CMOS) camera (Hamamatsu). Fixed microscopy was performed using a Nikon Ti microscope equipped with an epifluorescent source [either a mercury arc lamp (Prior) or an LED system (Lumencor)]; an automated stage (Prior); Cy3, Cy5, and DAPI filter sets (Chroma); and a CCD or CMOS camera (Hamamatsu).

Small-molecule screening

U2OS cells expressing p53-YFP and RFP (red fluorescent protein)–NLS (nuclear localization signal) were plated in plastic 96-well flat-bottom plates (Corning). Cells were grown for 24 hours and switched to transparent medium. Drugs were applied using an automated pinning system at the ICCB-Longwood Screening Facility. Plates for live imaging were then placed on a microscope, and imaging positions were determined. Imaging began immediately to determine a pre-NCS baseline 90 to 120 min after drug addition. NCS was added to each well, and the plates were imaged for 24 hours. Replicate plates were treated with NCS, left in the incubator for 10 hours, fixed with PFA and subsequently stained for p53, and imaged, and the antibody signal was quantified.

Microscopy data analysis

Microscopy data (live and fixed) were processed with a custom MATLAB code. Single cells were tracked manually using the phase images with a MATLAB interface. Single-cell tracks were projected onto the fluorescent images, which were then background-corrected (by median filtering and subsequent top-hat background subtraction), and nuclear signal (estimated as the average of the top 10 pixels in the nuclear area) was then computed for the applicable channels. For fixed images, the images were segmented using the DAPI channel with a watershed algorithm and mean nuclear intensity computed for each cell. Images displayed in the body of the paper were smoothed with a median or Gaussian filter and background-subtracted. Contrast was adjusted for optimal visualization and is consistent between pre- and posttreatment for all images. Automated tracking of U2OS cells was performed using a nuclear marker. Nuclei were identified in a given frame as objects with a given mCherry intensity, shape, and size. p53-YFP intensity was computed as the mean of the brightest 10 pixels within an identified region. Identified cells were connected across frames using a greedy nearest-neighbor algorithm resulting in single-cell traces.

Computational modeling

We constructed a four-species, 18-parameter model describing p53 oscillations driven by MDM2 transcription–based feedback using a delay differential equation framework. The two principal species, MDM2 and p53, were present in phosphorylated and nonphosphorylated forms. The phosphorylated MDM2 and p53 species had increased or decreased degradation rates, respectively. We performed all simulations in MATLAB (text S1).

SUPPLEMENTARY MATERIALS

www.sciencesignaling.org/cgi/content/full/10/476/eaah6671/DC1
Text S1. MATLAB simulations.
Fig. S1 Cell-to-cell variation in p53 abundance is not because of genetic inhomogeneity.
Fig. S2. Proliferation and induction of p53 target genes after DNA damage across cell lines.
Fig. S3. Characterization of modulators of p53 dynamics.
Fig. S4. The fraction of unrepaired DNA breaks is cell line–specific and does not depend on the damage dose.
Table S1. Summary of chemical screening data.

REFERENCES AND NOTES

1. C. Cohen-Saidon, A. A. Cohen, A. Sigal, Y. Liron, U. Alon, Dynamics and variability of ERK2 response to EGF in individual living cells. *Mol. Cell* **36**, 885–893 (2009).
2. N. Yissachar, T. Sharar Fischler, A. A. Cohen, S. Reich-Zeliger, D. Russ, E. Shifrut, Z. Porat, N. Friedman, Dynamic response diversity of NFAT isoforms in individual living cells. *Mol. Cell* **49**, 322–330 (2013).
3. R. L. Bar-Or, R. Maya, L. A. Segel, U. Alon, A. J. Levine, M. Oren, Generation of oscillation by the p53-Mdm2 feedback loop: A theoretical and experimental study. *Proc. Natl. Acad. Sci. U.S.A.* **97**, 11250–11255 (2000).
4. S.-H. Chen, G. Lahav, Two is better than one; toward a rational design of combinatorial therapy. *Curr. Opin. Struct. Biol.* **41**, 145–150 (2016).
5. G. Lahav, N. Rosenfeld, A. Sigal, N. Geva-Zatorsky, A. J. Levine, M. B. Elowitz, U. Alon, Dynamics of the p53-Mdm2 feedback loop in individual cells. *Nat. Genet.* **36**, 147–150 (2004).
6. J. E. Purvis, K. W. Karhohs, C. Mock, E. Batchelor, A. Loewer, G. Lahav, p53 dynamics control cell fate. *Science* **336**, 1440–1444 (2012).
7. X. Chen, J. Chen, S. Gan, H. Guan, Y. Zhou, Q. Ouyang, J. Shi, DNA damage strength modulates a bimodal switch of p53 dynamics for cell-fate control. *BMC Biol.* **11**, 73 (2013).
8. A. Loewer, K. Karanam, C. Mock, G. Lahav, The p53 response in single cells is linearly correlated to the number of DNA breaks without a distinct threshold. *BMC Biol.* **11**, 114 (2013).
9. D. A. Hamstra, M. S. Bhojani, L. B. Griffin, B. Laxman, B. D. Ross, A. Rehemtulla, Real-time evaluation of p53 oscillatory behavior in vivo using bioluminescent imaging. *Cancer Res.* **66**, 7482–7489 (2006).
10. Y. Shiloh, G. P. van der Schans, P. H. M. Lohman, Y. Becker, Induction and repair of DNA damage in normal and ataxia-telangiectasia skin fibroblasts treated with neocarzinostatin. *Carcinogenesis* **4**, 917–921 (1983).
11. E. Batchelor, C. S. Mock, I. Bhan, A. Loewer, G. Lahav, Recurrent initiation: A mechanism for triggering p53 pulses in response to DNA damage. *Mol. Cell* **30**, 277–289 (2008).
12. X. Wu, J. H. Bayle, D. Olson, A. J. Levine, The p53–mdm-2 autoregulatory feedback loop. *Genes Dev.* **7**, 1126–1132 (1993).
13. W. Lu, L. Chen, Y. Peng, J. Chen, Activation of p53 by roscovitine-mediated suppression of MDM2 expression. *Oncogene* **20**, 3206–3216 (2001).
14. Z. N. Demidenko, M. V. Blagosklonny, Flavopiridol induces p53 via initial inhibition of Mdm2 and p21 and, independently of p53, sensitizes apoptosis-reluctant cells to tumor necrosis factor. *Cancer Res.* **64**, 3653–3660 (2004).
15. J. Stewart-Ornstein, G. Lahav, Dynamics of CDKN1A in single cells defined by an endogenous fluorescent tagging toolkit. *Cell Rep.* **14**, 1800–1811 (2016).

16. R. Maya, M. Balass, S.-T. Kim, D. Shkedy, J.-F. Martinez Leal, O. Shifman, M. Moas, T. Buschmann, Z. Ronai, Y. Shiloh, M. B. Kastan, E. Katzir, M. Oren, ATM-dependent phosphorylation of Mdm2 on serine 395: Role in p53 activation by DNA damage. *Genes Dev.* **15**, 1067–1077 (2001).

17. S. Banin, L. Moyal, S.-Y. Shieh, Y. Taya, C. W. Anderson, L. Chessa, N. I. Smorodinsky, C. Prives, Y. Reiss, Y. Shiloh, Y. Ziv, Enhanced phosphorylation of p53 by ATM in response to DNA damage. *Science* **281**, 1674–1677 (1998).

18. P. Ye, Y. Liu, C. Chen, F. Tang, Q. Wu, X. Wang, C.-G. Liu, X. Liu, R. Liu, Y. Liu, P. Zheng, An mTORC1-Mdm2-Drosha axis for miRNA biogenesis in response to glucose- and amino acid-deprivation. *Mol. Cell* **57**, 708–720 (2015).

19. S. R. Peterson, A. Kurimasa, M. Oshimura, W. S. Dynan, E. M. Bradbury, D. J. Chen, Loss of the catalytic subunit of the DNA-dependent protein kinase in DNA double-strand-break-repair mutant mammalian cells. *Proc. Natl. Acad. Sci. U.S.A.* **92**, 3171–3174 (1995).

20. B. W. Durkacz, O. Omidiji, D. A. Gray, S. Shall, (ADP-ribose)$_n$ participates in DNA excision repair. *Nature* **283**, 593–596 (1980).

21. B. W. Durkacz, J. Irwin, S. Shall, Inhibition of (ADP-ribose)$_n$ biosynthesis retards DNA repair but does not inhibit DNA repair synthesis. *Biochem. Biophys. Res. Commun.* **101**, 1433–1441 (1981).

22. E. S. Yang, S. Nowsheen, T. Wang, D. K. Thotala, F. Xia, Glycogen synthase kinase 3β inhibition enhances repair of DNA double-strand breaks in irradiated hippocampal neurons. *Neuro Oncol.* **13**, 459–470 (2011).

23. P. Watcharasit, G. N. Bijur, J. W. Zmijewski, L. Song, A. Zmijewska, X. Chen, G. V. W. Johnson, R. S. Jope, Direct, activating interaction between glycogen synthase kinase-3β and p53 after DNA damage. *Proc. Natl. Acad. Sci. U.S.A.* **99**, 7951–7955 (2002).

24. A. Finzel, A. Grybowski, J. Strasen, E. Cristiano, A. Loewer, Hyperactivation of ATM upon DNA-PKcs inhibition modulates p53 dynamics and cell fate in response to DNA damage. *Mol. Biol. Cell* **27**, 2360–2367 (2016).

25. Z. Chen, S.-H. Yoo, Y.-S. Park, K.-H. Kim, S. Wei, E. Buhrd, Z.-Y. Ye, H.-L. Pan, J. S. Takahashi, Identification of diverse modulators of central and peripheral circadian clocks by high-throughput chemical screening. *Proc. Natl. Acad. Sci. U.S.A.* **109**, 101–106 (2011).

26. T. Hirota, J. Wook Lee, W. G. Lewis, E. E. Zhang, G. Breton, X. Liu, M. Garcia, E. C. Peters, J.-P. Etchegaray, D. Traver, P. G. Schultz, S. A. Kay, High-throughput chemical screen identifies a novel potent modulator of cellular circadian rhythms and reveals CKIα as a clock regulatory kinase. *PLOS Biol.* **8**, e1000559 (2010).

The following resources related to this article are available online at http://stke.sciencemag.org.
This information is current as of April 26, 2017.

Article Tools	Visit the online version of this article to access the personalization and article tools: http://stke.sciencemag.org/content/10/476/eaah6671
Supplemental Materials	*"Supplementary Materials"* http://stke.sciencemag.org/content/suppl/2017/04/21/10.476.eaah6671.DC1
Related Content	The editors suggest related resources on *Science*'s sites: http://stke.sciencemag.org/content/sigtrans/9/445/ra91.full http://stke.sciencemag.org/content/sigtrans/6/272/rs9.full http://stke.sciencemag.org/content/sigtrans/5/251/ra83.full
References	This article cites 26 articles, 12 of which you can access for free at: http://stke.sciencemag.org/content/10/476/eaah6671#BIBL
Permissions	Obtain information about reproducing this article: http://www.sciencemag.org/about/permissions.dtl